Astronomy & Astrophysics manuscript no. paper_dornHinkel
January 9, 2017
©ESO 2017

Bayesian analysis of interiors of HD 219134b, Kepler-10b, Kepler-93b, CoRoT-7b, 55 Cnc e, and HD 97658b using stellar abundance proxies

Caroline Dorn[1], Natalie R. Hinkel[2], and Julia Venturini[1]

[1] Physics Institute, University of Bern, Sidlerstrasse 5, CH-3012, Bern, Switzerland
e-mail: caroline.dorn@space.unibe.ch
[2] School of Earth & Space Exploration, Arizona State University, Tempe, AZ 85287, USA

arXiv:1609.03909v2 [astro-ph.EP] 6 Jan 2017

January 9, 2017

ABSTRACT

Aims. Using a generalized Bayesian inference method, we aim to explore the possible interior structures of six selected exoplanets for which planetary mass and radius measurements are available in addition to stellar host abundances: HD 219134b, Kepler-10b, Kepler-93b, CoRoT-7b, 55 Cnc e, and HD 97658b. We aim to investigate the importance of stellar abundance proxies for the planetary bulk composition (namely Fe/Si and Mg/Si) on prediction of planetary interiors.
Methods. We performed a full probabilistic Bayesian inference analysis to formally account for observational and model uncertainties while obtaining confidence regions of structural and compositional parameters of core, mantle, ice layer, ocean, and atmosphere. We determined how sensitive our parameter predictions depend on (1) different estimates of bulk abundance constraints and (2) different correlations of bulk abundances between planet and host star.
Results. The possible interior structures and correlations between structural parameters differ depending on data and data uncertainty. The strongest correlation is generally found between size of rocky interior and water mass fraction. Given the data, possible water mass fractions are high, even for most potentially rocky planets (HD 219134b, Kepler-93b, CoRoT-7b, and 55 Cnc e with estimates up to 35 %, depending on the planet). Also, the interior of Kepler-10b is best constrained with possible interiors similar to Earth. Among all tested planets, only the data of Kepler-10b and Kepler-93b allow to put a higher probability on the planetary bulk Fe/Si to be stellar compared to extremely sub-stellar.
Conclusions. Although the possible ranges of interior structures are large, structural parameters and their correlations are constrained by the sparse data. The probability for the tested exoplanets to be Earth-like is generally very low. Furthermore, we conclude that different estimates of planet bulk abundance constraints mainly affect mantle composition and core size.

Key words. exoplanet interior – constrained interior structure – stellar abundance constraints – HD 219134b –Kepler-10b – Kepler-93b – CoRoT 7b – 55 Cnc e – HD 97658b

1. Introduction

The characterization of exoplanet interiors is key to understand planet diversity. Here we focus on characterizing six exoplanets for which mass, radius, and also refractory element abundances of the stellar hosts are known. These exoplanets are HD 219134b, Kepler-10b, Kepler-93b, CoRoT-7b, 55 Cnc e, and HD 97658b. In order to make meaningful statements about their interior structures, it is mandatory not only to find few interior realizations that explain the data, but also to quantify the spread in possible interior structures that are in agreement with data, and data and model uncertainty (Rogers & Seager 2010; Dorn et al. 2015, 2017). This spread is generally large, due to the inherent degeneracy, i.e. different interior realizations can have identical mass and radius. We therefore apply the methodology presented by Dorn et al. (2017) that employs a full probabilistic Bayesian inference analysis using a Markov chain Monte Carlo (McMC) method. This method is validated against Neptune and previously by Dorn et al. (2015) against the terrestrial fitsyno planets. It allows us to determine confidence regions for structural and compositional parameters of core, mantle, ice layer, ocean, and atmosphere.

Planet bulk abundance constraints, in addition to mass and radius, are crucial to reduce the generally high degeneracy in interior structures (Dorn et al. 2015; Grasset et al. 2009). Stellar abundances in relative refractory elements (Fe/Si and Mg/Si) were suggested to serve as a proxy for the planetary abundance (e.g., Bond et al. 2010; Elser et al. 2012; Johnson et al. 2012; Thiabaud et al. 2015). Spectroscopic observations of relative photospheric abundances of host stars may allow us to determine their importance for the interior characterization of planetary companions as outlined by Santos et al. (2015). We proceed along these lines and study the sensitivity of interior parameter predictions to different planet bulk abundances by testing (1) different stellar abundance estimates and (2) different correlations between stellar and planetary abundance ratios.

Over the last few decades, a variety of telescopes and spectrographs have been utilized to measure stellar abundances, which affects the resolution and signal-to-noise (S/N) ratios of the data. In addition, the techniques used to determine the element abundances differ. Then, each research group chooses their own line list and number of ionization stages included, solar atmosphere models, and adopted solar abundances. All of these differences result in element abundance measurements that are

fundamentally on different baselines and which do not overlap to within error (Hinkel et al. 2014). Here, we investigate whether these discrepancies significantly affects the determination of interior structure or not.

The six selected exoplanets for which host star abundances are available have bulk densities in the range from 6.8 g/cm^3 (Kepler-93b) to 3.4 g/cm^3 (HD 97658b) and span across the proposed transition range between mostly rocky and mostly non-rocky exoplanets (e.g., Lopez & Fortney 2013; Rogers 2015). Terrestrial-type planets are generally thought to be differentiated with an iron-rich core, a silicate mantle, and a crust, whereas volatile-rich planets are thought to also contain significant amount of ices and/or atmospheres (e.g., see Howe et al. 2014). Direct atmosphere characterization for the selected planets are not available, except for the only recently characterized atmosphere of 55 Cnc e (Tsiaras et al. 2016; Demory et al. 2015). For super Earths in general, the diversity of atmospheric structures and compositions are mostly theoretical (e.g., see Burrows 2014, for a review). Studies of mass-radius relations generally consider H_2-He atmospheres (e.g., Rogers et al. 2011; Fortney et al. 2007) and H_2O as liquid and high pressure ice (e.g., Valencia et al. 2007; Seager et al. 2007). However, compositional diversity of atmospheres and ices in planets may exceed the one found in our solar system (e.g., Newsom 1995). But the sparse observational data on exoplanets will only allow us to constrain few structural and compositional parameters. In that light, we assume a general planetary structure of a pure iron core, a silicate mantle, a water layer, and an atmosphere made of H, He, C, and O. Given the data, we constrain core size, mantle thickness and composition, mass of water, and key characteristics of the atmosphere (mass fraction, luminosity, and metallicity). Here, we use the term atmosphere synonymously with gas layer, for which there is commonly a distinction between a convective (i.e., envelope) and a radiative part (i.e., atmosphere).

In order to compute the structure for a planet of a given interior, we employ model I from Dorn et al. (2017). Namely, we employ state-of-the-art structural models that compute irradiated atmospheres and self-consistent thermodynamics of core, mantle, high-pressure ice and ocean.

This paper is organized as follows: in Section 2 we review previous interior studies on the planets of interest. In Section 3 we introduce the inference strategy, model parameters, data and the physical model that links data and model parameters. In Section 4, we apply our method on the six selected exoplanets and test different stellar abundance proxies for constraints on planet bulk abundance. We end with discussion and conclusions.

2. Previous studies of the selected exoplanets

Previous estimates on the interiors of HD 219134b, Kepler-10b, Kepler-93b, CoRoT-7b, 55 Cnc e, and HD 97658b generally do not comprehensively reflect the inherent degeneracy that different interiors can explain the observations. Often a few interior scenarios are discussed but it remains unclear how well specific models compare with the generally large number of possible scenarios. Commonly used mass-radius curves of idealized compositions plotted against the planetary data (Figure 1) allow a general evaluation whether a planet can either be composed of pure rocks or is volatile-rich.

For Kepler-10b, Batalha et al. (2011) estimate a predominantly rocky composition of iron and silicates, with a mass fraction of water that can be as high as 25 %. With the additional constraint of maximum mantle stripping during planet formation (Marcus et al. 2009), they predict a dry iron-rich interior.

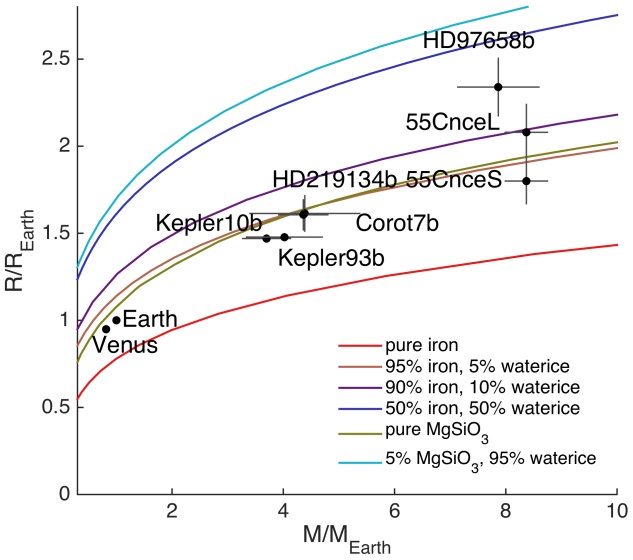

Fig. 1. Masses and radii of the six exoplanets of interest, including two scenarios for 55Cnc e (see main text). The terrestrial solar system planets are also plotted against idealized mass-radius curves of pure iron, pure magnesium silicate, and a 2-layered composition of 5 % magnesium silicate and 95 % water.

For both Kepler-10b and CoRoT-7b, Wagner et al. (2012) argue for a large iron core similar to Mercury (∼60 % iron and ∼30 % silicates), whereas Dressing et al. (2015); Weiss et al. (2015) suggest an Earth-like interior (17 % iron and 83 % silicates). The latter conclusion also holds for Kepler-93b (Dressing et al. 2015). For Kepler-10b and CoRoT-7b it remains unclear if they may or may not be remnants of larger volatile-rich planets that have lost their atmospheres (e.g., Kurokawa et al. 2013; Valencia et al. 2010).

We find that HD 219134b is very similar in size and mass to CoRoT-7b. Compared to CoRoT-7b, HD 219134b has higher precision on mass and radius and it receives less energy from its host star. Given a bulk density of 5.76 g/cm^3, Motalebi et al. (2015) suggest a rocky composition and describe a best fit two-component model of iron-magnesium silicate mantle (77 %) and a core mass fraction of approximately 23 %.

The bulk density of 55 Cnc e (R = 2.0 $R_\oplus$) is too low to be made of pure rocks and needs to contain significant mass of water, gas, or other light elements (Winn et al. 2011), although Gillon et al. (2012) argue that any kind of atmosphere is unlikely due to the intense stellar irradiation. Previous estimates of water mass fractions that can explain the data are e.g., ∼ 45 % (Endl et al. 2012) or ∼ 20 % (Gillon et al. 2012). We note that both estimates are based on differently assumed bulk densities and rock/silicate partitions. Recent infrared monitoring revealed a high surface temperature difference between day and night side which implies either an optically thick atmosphere with heat recirculation confined to the planetary dayside or no atmosphere (Demory et al. 2016). Also, recent spectroscopic observations have suggested a hydrogen-rich atmosphere (Tsiaras et al. 2016). For 55 Cnc e, different radii can be found in the literature (Demory et al. 2015, and references therein). Here, we simply distinguish two cases 55 Cnc e^L (R = 2.08 $R_\oplus$) and 55 Cnc e^S (R = 1.75 $R_\oplus$), where the superscripts refer to small (S) and large (L), both of which can be seen in Figure 1.

The least dense and irradiated exoplanet in this study, HD 97658b, can be explained by a rocky core of at least 60 %

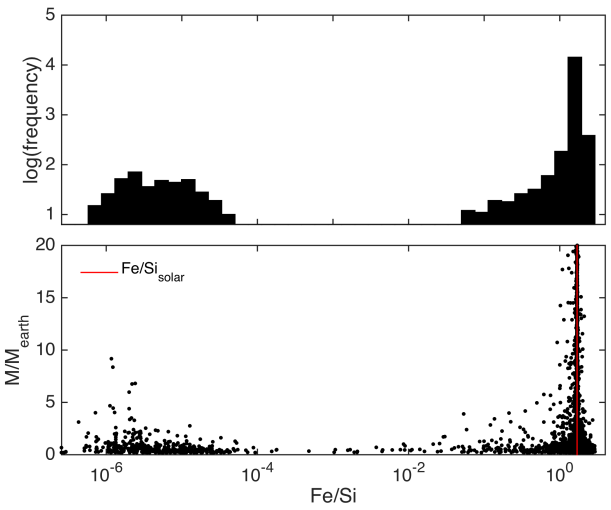

Fig. 2. Top: Histogram of bulk Fe/Si of $\sim$ 15400 simulated planets that accreted from discs of solar composition. Bottom: planet mass over bulk Fe/Si of the same simulations (10 planet embryos were used in each simulation). Note the log-scale. The distribution of planets is a result from Thiabaud et al. (2015).

in mass with an envelope of lighter elements and little H-He components, at most 2 % by mass (Van Grootel et al. 2014). But its density is also consistent with a water-dominated planet (Dragomir et al. 2013).

3. Methodology

We use the methodology of Dorn et al. (2017, model I) that determines possible ranges of interiors which can include thin and thick atmospheres. We outline the main aspects of the method in the following.

3.1. Bayesian inference

We employ a Bayesian method to compute the posterior probability density function (pdf) of the model parameter conditional on the data and prior information. The prior probability of the model represents the information known about the interior structure before using data. According to Bayes' theorem, the posterior distribution for a fixed model parametrization, conditional on data, is proportional to prior information on model parameters and the likelihood function. The likelihood function summarizes the distance (typically a norm of a vector of residuals) between the model simulation and observed data. It is practically impossible to analytically derive the posterior distribution since the addressed problem is high-dimensional and non-linear and data are sparse. We therefore employ a McMC sampling method that iteratively searches the prior parameter space and locally evaluates the likelihood function. Samples of model parameters that are generated with this approach are distributed according to the underlying posterior distribution. As in Dorn et al. (2017), we use the Metropolis-Hastings algorithm to efficiently explore the posterior distribution. We refer to Dorn et al. (2015) and Dorn et al. (2017) for more details.

The large number of models that is needed for the analysis requires very efficient computations. In our work, generating the planet's internal structure takes on average 40 - 90 seconds of CPU time on a four quad-core AMD Opteron 8380 CPU node and 32 GB of RAM. In all, we sampled about 10^6 models and retained around 5×10^4 models for further analysis.

3.2. Bulk abundance constraints

Theoretical and empirical evidences suggest that relative abundances of refractory elements are correlated between star and planet. For example, there is a high similarity among Fe/Si and Mg/Si for Sun, Earth, Mars, the Moon as well as meteorites (Lodders 2003; Drake & Righter 2002; McDonough & Sun 1995; Khan & Connolly 2008; Kuskov & Kronrod 2001), which are believed to represent building blocks of planets (Morgan & Anders 1980). Planet formation studies have demonstrated that there are direct correlations among relative refractory element abundances (e.g., Fe, Mg, and Si) between star and hosted planets (e.g., Bond et al. 2010; Elser et al. 2012; Johnson et al. 2012; Thiabaud et al. 2015). This is because refractory elements Fe, Si, and Mg condense at similar temperatures corresponding to small distances from the host star ($\gtrsim$ 0.06 AU).

Thiabaud et al. (2015) verified the direct correlation for a wide range of stellar compositions. For their tested solar-like disk composition (e.g., $\mathrm{Fe/Si_{Sun}}$ = 1.69, $\mathrm{Mg/Si_{Sun}}$ = 0.89), the full distribution of planetary bulk Fe/Si is shown in Figure 2. For the subset of planets with semi-major axes below 0.1 AU, the distribution is very weakly bimodal with 8 % of all planets having a very low iron content (Fe/Si < 0.001). For this particular solar-like disk composition, the authors showed that at close distances to the star (0 – 0.2 AU), the disk's Fe/Si (10^{-6}–10^{-4}) and Mg/Si (0.08–4) mass ratios can significantly differ from solar values (see also Figure 3 in Thiabaud et al. 2015). This is because the condensation conditions differ among Mg-Si-Fe-bearing species. This seems to indicate that a small fraction of planets that accrete material from respective regions may have very low iron content. Here, we test the sensitivity of our interior predictions on such extremely different stellar abundance proxies for the planetary bulk composition (see section 4.3):

- direct abundance proxy:
  $\mathrm{Fe/Si_{bulk}} = \mathrm{Fe/Si_{star}}$
  $\mathrm{Mg/Si_{bulk}} = \mathrm{Mg/Si_{star}}$

- non-direct abundance proxy:
  $\mathrm{Fe/Si_{bulk}} = 10^{-5}\ \mathrm{Fe/Si_{star}}$
  $\mathrm{Mg/Si_{bulk}} = 0.5\ \mathrm{Mg/Si_{star}}$

We note that Thiabaud et al. (2015) does neglect the drift of planetesimals, which may lead to an underestimation of bulk Fe/Si in their simulated planets. Future studies need to improve our understanding of the evolution of element ratios.

3.3. Stellar abundance data

We have culled stellar abundances from multiple datasets for HD 219134, 55 Cnc e, and HD 97658b and homogenized them via the Hypatia Catalog (Hinkel et al. 2014). In order to properly compare the datasets with each other, we have renormalized the abundances to the Lodders et al. (2009) solar abundance scale. To maintain coherence between abundance measurements, our analysis did not take into consideration groups who utilized NLTE (non-local thermodynamic equilibrium) approximations. The different stellar abundance estimates of 55 Cnc e, HD 97658, and HD 219134 are listed in Table 1. For Kepler-10 b, Kepler-93 b, and CoRoT-7 b, the stellar abundances have only been determined by one group, that is Santos et al. (2015).

Note, ratios with squared brackets ([X/H], e.g., Table 1) are logarithmic particle ratios in reference to the Sun. The majority of our discussion is with respect to abundance mass ratios without reference to the Sun (X/H, e.g., Table 3).

Table 1. Stellar abundances. The unit is dex (see Appendix A).

parameter	HD 219134	55 Cnc	HD 97658
$[\mathrm{Fe/H}]$	0.04–0.84	0.29– 0.67	-0.05 – -0.28
$[\mathrm{Fe/H}]_{\mathrm{median}}$	0.13	0.44	-0.13
$[\mathrm{Mg/H}]$	0.09–0.37	0.34 –0.80	-0.18 – -0.27
$[\mathrm{Mg/H}]_{\mathrm{median}}$	0.32	0.41	-0.22
$[\mathrm{Si/H}]$	0.04–0.27	0.29 –0.57	-0.20 – -0.28
$[\mathrm{Si/H}]_{\mathrm{median}}$	0.12	0.40	-0.21
$[\mathrm{Na/H}]$	0.17–0.32	0.23– 0.63	-0.24 – -0.26
$[\mathrm{Na/H}]_{\mathrm{median}}$	0.19	0.49	-0.25
$[\mathrm{Al/H}]$	0.16–0.29	0.43–0.55	-0.23
$[\mathrm{Al/H}]_{\mathrm{median}}$	0.23	0.51	-0.23
$[\mathrm{Ca/H}]$	0.18–0.25	0.09 –0.46	-0.25
$[\mathrm{Ca/H}]_{\mathrm{median}}$	0.21	0.24	-0.25

The abundances for HD 219134, which is located 6.55 pc from the Sun, were measured by a total of 9 groups within the literature. The maximum [Fe/H] determination was by Mishenina et al. (2015) with 0.84 dex, while Ramirez et al. (2007) measured a minimum of 0.04 dex and the median was 0.13 dex. Only three groups measured [Mg/H], where we use the median value of 0.32 dex and spread of 0.28 dex. The [Si/H] ratio spanned 0.04 dex per Valenti & Fischer (2005) to 0.27 dex (Thevenin 1998, Thevenin & Idiart 1999), with a median of 0.12 dex between the five contributing groups. The sodium, aluminum, and calcium abundance ratios were measured by three groups or less. The median for [Na/H] is 0.19 dex and [Al/H] is 0.23 dex, both with a spread of 0.13 dex. The [Ca/H] measurements had a smaller spread with 0.07 dex, while the median was 0.21 dex.

A total of 18 groups measured element abundances for 55 Cnc, which is 12.34 pc from the Sun. The [Fe/H] measurements ranged from 0.29 dex (Mishenina et al. 2004) to 0.67 dex (Takeda et al. 2007), with a median of 0.44 dex. Of the 18 groups, six of them measured [Mg/H], where the minimum determination was 0.34 dex (Delgado Mena et al. 2010), the maximum was 0.80 dex (Allende Prieto et al. 2004), and the median was 0.41 dex. The [Si/H] ratio was determined by 11 measurements and spanned 0.29 dex (Gonzalez et al. 2001) to 0.57 dex (Allende Prieto et al. 2004), with a median of 0.40 dex. The sodium abundance ratio varied from 0.23 dex (Gonzalez et al. 2001) to 0.63 dex per Shi et al. (2004) out of eight datasets, where the median was 0.49 dex. The [Al/H] determinations were only measured by five groups who ranged from 0.43 dex (Kang et al. 2011) to 0.55 dex (Luck & Heiter 2005) and a median of 0.51 dex. Finally, [Ca/H] was measured by 7 groups, with a minimum of 0.09 dex (Zhao et al. 2002) to a maximum of 0.46 dex (Luck & Heiter 2005); the median is 0.24 dex.

HD 97658 is a star 21.11pc away from the Sun and was spectroscopically observed by six different groups. The variation in [Fe/H] goes from -0.05 (Petigura et al. 2011) to -0.28 dex (Mishenina et al. 2008) with a median value of -0.13 dex. The [Mg/H] ratio was only measured by two groups: Mishenina et al. (2008) and Mortier et al. (2013) who determined -0.18 dex and -0.27 dex, respectively. Three groups measured [Si/H] in HD 97658 and had a variation spanning -0.20 dex (Valenti & Fischer 2005) to -0.28 dex (Mortier et al. 2013), with a median of -0.21 dex. Both Mortier et al. (2013) and Valenti & Fischer (2005) determined [Na/H], citing -0.24 dex and -0.26 dex, respectively. Finally, only Mortier et al. (2013) measured [Al/H] = -0.23 dex and [Ca/H] = -0.25 dex.

For the host stars HD 219134, 55 Cnc, and HD 97658, we adopt three scenarios for their abundances: a case representing the median estimate from different studies (V0), an iron-rich (V1) and an iron-poor (V2) case. Whenever unspecified, the reference scenario V0 is used. For the three cases, we compile stellar abundance estimates in Table 2 based on Table 1. These stellar abundance estimates serve as proxies for the planet bulk abundance (see Table 3, columns 3–7). In section 4.2 we examine how the spread of bulk abundance constraints influence our predictions on the planetary interiors of HD 219134b, 55 Cnc e, and HD 97658b.

3.4. Data

The data **d** that we rely on to constrain planetary interiors (see section 3.1) are:

- planetary mass M,
- planetary radius R,
- bulk planetary ratio $\mathrm{Fe/Si_{bulk}}$,
- bulk planetary ratio $\mathrm{Mg/Si_{bulk}}$,
- mantle composition of minor elements: CaO, Al_2O_3, Na_2O,
- semi-major axis,
- stellar radius R_{star},
- stellar effective temperature T_{star}.

Table 3 lists all data for the six selected exoplanets. Figure 1 shows their masses and radii plotted against M-R-curves of idealized compositions.

The $\mathrm{Fe/Si_{bulk}}$ mass ratio relates the mass of iron to silicon for the entire planet (core and mantle). Since all magnesium and silicate are in the mantle, $\mathrm{Mg/Si_{bulk}}$ equals $\mathrm{Mg/Si_{mantle}}$. As stated earlier, we are using two stellar abundance proxies, that is direct and non-direct proxy (section 3.2). Following Dorn et al. (2015), we fix absolute abundances of minor refractories in the mantle (oxides of Ca, Na, and Al) to the stellar proxy. The system of Na_2O–CaO–FeO–MgO–Al_2O_3–SiO_2 is chosen, because it is able to explain 99% of Earth's mantle. Whenever stellar proxies of these minor compounds are not available, we assume chondritic abundances from Lodders et al. (2009). Semi-major axis, stellar radius, and stellar effective temperature are also fixed parameters.

3.5. Model parametrization

Our exoplanet interior model consists of an iron core surrounded by a silicate mantle, a water layer and a gas layer as illustrated in Figure 3. The key structural model parameters **m** that we aim to constrain are:

- core radius r_{c},
- mantle $\mathrm{Fe/Si_{mantle}}$,
- mantle $\mathrm{Mg/Si_{mantle}}$,
- mantle radius r_{mantle},
- mass of water m_{water},
- mass of atmosphere m_{env},
- atmosphere Luminosity L,
- atmosphere metallicity Z_{env},

where Z_{env} is defined as the atmosphere mass fraction of elements heavier than H and He (here C and O).

Table 2. Compiled stellar abundances representing median estimate from different studies (V0), an iron-rich (V1) and an iron-poor (V2) case. The unit is dex.

parameter	HD 219134			55 Cnc			HD 97658		
	V0	V1	V2	V0	V1	V2	V0	V1	V2
[Fe/H]	0.13	0.84	0.04	0.44	0.67	0.29	-0.13	-0.05	-0.28
[Mg/H]	0.32	0.09	0.37	0.41	0.34	0.8	-0.22	-0.27	-0.18
[Si/H]	0.12	0.04	0.27	0.40	0.29	0.57	-0.21	-0.28	-0.2
[Na/H]	0.19	0.17	0.32	0.49	0.23	0.63	-0.25	-0.24	-0.26
[Al/H]	0.23	0.16	0.29	0.51	0.43	0.55	-0.23	-0.23	-0.23
[Ca/H]	0.21	0.18	0.25	0.24	0.09	0.46	-0.25	-0.25	-0.25

Table 3. Data of selected exoplanets. V0 represents median abundance estimates, whereas V1 and V2 refer to iron-rich and iron-poor cases as listed in Table 2; indices L and S of 55 Cnc e refer to different radius estimates (see section 2).

name	M [$M_\oplus$]	R [$R_\oplus$]	Fe/Si_{bulk}	Mg/Si_{bulk}	Na_2O [wt%]	Al_2O_3 [wt%]
HD 219134 b (V0)	4.36 ± 0.44	1.606 ± 0.086	1.73±1.55	1.44±0.91	0.021	0.055
HD 219134 b V1	4.36 ± 0.44	1.606 ± 0.086	10.68±1.55	1.02±0.91	0.01	0.023
HD 219134 b V2	4.36 ± 0.44	1.606 ± 0.086	1.00±1.55	1.14±0.91	0.025	0.057
Kepler 10-b	3.7 ± 0.43	1.47 ± 0.02	2.18±0.41	1.14±0.28	0.02	0.05
Kepler 93-b	4.02 ± 0.68	1.478 ± 0.019	2.87±0.98	1.02±0.38	0.02	0.05
CoRoT 7-b	4.386 ± 0.985	1.614 ± 0.102	2.34±0.68	0.87±0.25	0.02	0.05
HD 97658b (V0)	7.866 ± 0.73	2.340 ± 0.165	2.03±1.17	0.87±0.33	0.018	0.046
HD 97658b V1	7.866 ± 0.73	2.340 ± 0.165	2.87±1.17	0.93±0.33	0.018	0.045
HD 97658b V2	7.866 ± 0.73	2.340 ± 0.165	1.41±1.17	0.95±0.33	0.019	0.05
55 Cnc e^L (V0)	8.37 ± 0.38	2.08 ± 0.16	1.86±1.49	0.93±0.77	0.024	0.062
55 Cnc e^S (V0)	8.37 ± 0.38	1.75 ± 0.13	1.86±1.49	0.93±0.77	0.024	0.062
55 Cnc $e^{S/L}$V1	8.37 ± 0.38	1.75 ± 0.13 / 2.08 ± 0.16	4.06±1.49	1.02±0.77	0.012	0.046
55 Cnc $e^{S/L}$ V2	8.37 ± 0.38	1.75 ± 0.13 / 2.08 ± 0.16	0.89±1.49	1.54±0.77	0.024	0.048

name	CaO [wt%]	R_{star} [R_{sun}]	T_{star} [T_{sun}]	semi-major axis [AU]
HD 219134 b (V0)	0.021	0.778	0.815	0.038
HD 219134 b V1	0.01	0.778	0.815	0.038
HD 219134 b V2	0.021	0.778	0.815	0.038
Kepler 10-b	0.02	1.065	0.978	0.017
Kepler 93-b	0.02	0.919	0.983	0.054
CoRoT 7-b	0.02	0.870	0.921	0.017
HD 97658b (V0)	0.017	0.703	0.887	0.08
HD 97658b V1	0.017	0.703	0.887	0.08
HD 97658b V2	0.019	0.703	0.887	0.08
55 Cnc e^L (V0)	0.013	0.943	0.901	0.015
55 Cnc e^S (V0)	0.013	0.943	0.901	0.015
55 Cnc $e^{S/L}$V1	0.008	0.943	0.901	0.015
55 Cnc $e^{S/L}$ V2	0.016	0.943	0.901	0.015

3.6. Structure model

Data $\mathbf{d}$ and model parameters $\mathbf{m}$ are linked by a physical model embodied by the forward operator $g(\cdot)$:

$$\mathbf{d} = g(\mathbf{m})\,. \tag{1}$$

For a given model $\mathbf{m}$, the interior structure (density profile), total mass M, transit radius R, and Fe/Si_{bulk} are computed for the purpose of comparing with observed data $\mathbf{d}$. The function $g(\mathbf{m})$ is computed combining thermodynamic and Equation-of-State (EoS) modeling which is adopted from Dorn et al. (2017). In the following, we briefly summarize the detailed description given in Dorn et al. (2017, model I).

Iron core For the core density profile, we use the EoS fit of iron in the hcp (hexagonal close-packed) structure provided by Bouchet et al. (2013) on *ab initio* molecular dynamics simulations for pressures up to 1500 GPa. This EoS fit is optimal for the modeling of Earth-like exoplanets up to ten Earth masses. The temperature gradient is assumed to be adiabatic.

Silicate mantle We employ a self-consistent thermodynamic method within the Na_2O-CaO-FeO-MgO-Al_2O_3-SiO_2 model system. We assume thermodynamic equilibrium. Equilibrium mineralogy and density are computed as a function of pressure, temperature, and bulk composition by Gibbs energy minimization (Connolly 2009). For these calculations the pressure is ob-

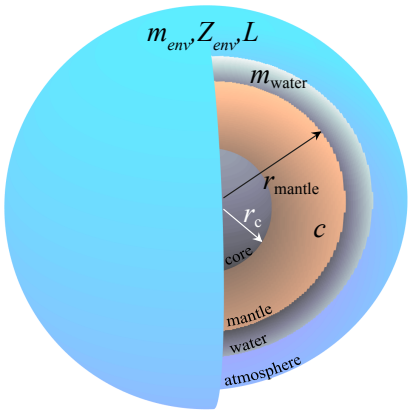

Fig. 3. Illustration of model parametrization. Model parameters are core radius $r_{\rm c}$, mantle composition c comprising the oxides Na_2O–CaO–FeO–MgO–Al_2O_3–SiO_2, mantle radius $r_{\rm mantle}$, mass of water $m_{\rm water}$, mass of atmosphere $m_{\rm env}$, atmosphere Luminosity L, and atmosphere metallicity $Z_{\rm env}$.

tained by integrating the load from the surface boundary, while temperature is obtained by integrating an Earth-like temperature gradient from the surface temperature of the mantle. This surface temperature equals the temperature at the bottom of the water layer.

Water layer In order to compute the density profile of the water layer, we follow Vazan et al. (2013) using a quotidian equation of state (QEOS). This QEOS is in good agreement with widely used ANOES (Thompson & Lauson 1972) and SESAME EoS (Lyon & Johnson 1992). Above 44.3 GPa, we use the tabulated EoS from Seager et al. (2007) that is derived from DFT simulations and predict a gradual transformation from ice VIII to X. We assume an adiabatic temperature profile.

Gas envelope and atmosphere model For a given radius and mass of the solid interior, distance to the star a, stellar effective temperature $T_{\rm star}$, stellar radius $R_{\rm star}$, envelope luminosity L, gas metallicity $Z_{\rm env}$, and gas mass $m_{\rm env}$, we solve the equations of hydrostatic equilibrium, mass conservation, and energy transport. As in Venturini et al. (2015), we implement the CEA (Chemical Equilibrium with Applications) package (Gordon & McBride 1994) for the EoS, which performs chemical equilibrium calculations for an arbitrary gaseous mixture, including dissociation and ionisation, and assuming ideal gas behavior. We account for gas compositions of H, He, C and O which are key atmospheric elements.

An irradiated atmosphere is assumed at the top of the gaseous envelope, for which the analytic irradiation model of Guillot et al. (2010) is adopted. This irradiation model assumes a semi-gray, global temperature averaged profile. The temperature is defined by envelope luminosity L and stellar irradiation. For the planets of interest, internal temperatures generally range between 1000 and 3000 K, intrinsic heat fluxes from the interior lie between 10 and 350 K. Calibrated opacities for different equilibrium temperatures and solar metallicities from Jin et al. (2014) are used. When non-solar metallicities are considered ($Z_{\rm env} \neq 0.02$), computed opacities are thus not self-consistent (see discussion in section 5).

The boundary between the irradiated atmosphere and the envelope is defined where the optical depth in visible wavelengths is much larger than 1 (Jin et al. 2014). Within the envelope, the usual Schwarzschild criterion is used to distinguish between convective and radiative layers. That is, if the adiabatic temperature gradient is larger than the radiative one, the layer is stable against convection. In order to compute the planet radius of a model realization we evaluate where the chord optical depth becomes 2/3 (Guillot et al. 2010). This allows us to compare calculated planet radii with measured radii from primary transits.

3.7. Prior information

Table 4 lists the ranges of prior information. Reasonable choices for the prior distributions are crucial such that we do not arbitrarily favor certain model realizations without justification. We have adopted the prior ranges from Dorn et al. (2017).

Prior bounds on $\rm Fe/Si_{mantle}$ and $\rm Mg/Si_{mantle}$ are linked to the host star's photospheric abundances. Since all Si and Mg are assumed to be in the mantle, $\rm Mg/Si_{star}$ defines the prior bounds on $\rm Mg/Si_{mantle}$, while $\rm Mg/Si_{star}$ is Gaussian-distributed. The iron content, on the other hand, is distributed between core and mantle. Thus, the bulk constraint $\rm Fe/Si_{bulk}$ defines only the upper bound of the prior on $\rm Fe/Si_{mantle}$. There is also a numerical constraint that the absolute iron oxide abundance in the mantle cannot exceed 70 %. For $m_{\rm env}$ and L, we assume a Jeffrey's prior, i.e., the logarithm of the parameter is uniformly distributed.

Table 4. Prior ranges of model parameters.

parameter	prior range
$r_{\rm c}$	0 – R (uniform in $r_{\rm core}^3$)
$\rm Fe/Si_{mantle}$	0 – $\rm Fe/Si_{star}$(uniform)
$\rm Mg/Si_{mantle}$	$\rm Mg/Si_{star}$ (Gaussian)
$r_{\rm mantle}$	0 – 1.1 R (uniform)
$m_{\rm water}$	0 – 0.99 M (uniform)
$m_{\rm env}$	10^{-12} $M_\oplus$– 0.9 M (Jeffrey's prior)
L	10^{18} – 10^{23} erg/s (Jeffrey's prior)
$Z_{\rm env}$	0 – 1 (uniform in $Z_{\rm env}{}^{-1}$)

4. Results

We apply our method to the six selected exoplanets with the data listed in Table 3 and first assume the direct abundance proxy ($\rm Fe/Si_{bulk} = Fe/Si_{star}$ and $\rm Mg/Si_{bulk} = Mg/Si_{star}$) and best guess stellar abundance estimates. We calculated the posterior distribution of model parameters and analyzed 2-dimensional (2-D) correlations between all 8 model parameters. In the following, we highlight a few (2-D) parameter correlations: $r_{\rm mantle}$, $r_{\rm c}$, and $\rm Fe/Si_{mantle}$ (Figure 4), $r_{\rm mantle}$ and $m_{\rm water}$ (Figure 5); $r_{\rm c}$ and $m_{\rm water}$ (Figure 6), as well as $Z_{\rm env}$ and atmospheric radius fraction $r_{\rm env}/R$ (Figure 7).

The correlation between mantle composition and core size (Figure 4) is introduced by the bulk abundance constraint $\rm Fe/Si_{bulk}$. For planets for which the uncertainty on $\rm Fe/Si_{star}$ is lowest (below 34 %), namely Kepler-10b, Kepler-93b, and CoRoT-7b, an increase in core-size leads to lower mantle $\rm Fe/Si_{mantle}$ in order to fit bulk abundance constraints. This is illustrated by the horizontal shift in color (Figure 4b-d) from yellow to blue. Whenever $\rm Fe/Si_{star}$ has a large uncertainty (e.g., about 90 %, 80 %, and 60 % for HD 219134b, 55 Cnc, and

HD 97658, respectively), the negative correlation between mantle size and mantle $\mathrm{Fe/Si_{mantle}}$ dominates. In these cases the color shifts from yellow to blue vertically. This is because the dominating datum is mass. More specifically, the core size is less well constrained, because for example a decrease in mantle size can be compensated by increasing $\mathrm{Fe/Si_{mantle}}$ in order to fit mass without affecting r_{c}. For HD 97658b, actually both trends are visible, yellow roughly shifts along a diagonal.

The correlation between r_{mantle} and m_{water} is generally strong as depicted in Figure 5. As expected from comparisons to idealized mass-radius-curves (see Figure 1), it is possible to explain the data for HD 219134b, Kepler-10b, Kepler-93b, CoRoT-7b, and 55 Cnc $\mathrm{e^S}$ with a rocky interior and no significant volatile layer. The full posterior range of the water mass fraction, however, reveals that significant volatile compounds cannot be excluded by the data. The possible mass fraction of water,m_{water}, spans from 0–35 % (0–17 % to explain the data within 1-σ uncertainty) depending on the planet. Thus, their probability to be Earth-like is low, also since posterior distributions are generally large. Only for Kepler-10b the range of possible water mass fractions is restricted to maximum few percents. For the least dense exoplanets 55 Cnc $\mathrm{e^L}$ and HD 97658b, m_{water} can be as large as 0.7 M and 0.95 M, respectively (0.3 M and 0.7 M, respectively, to fit the data within 1-σ uncertainty, blue points in Figure 5).

Also, the (negative) correlation between mantle size r_{mantle} and m_{water} for all planets (Figure 5) is much stronger than between core size r_{c} and m_{water} (Figure 6). More specifically, this is because the parameters that most strongly affect planet mass are r_{mantle} and m_{water}. An increase in r_{mantle} can be compensated by decreasing m_{water}, while still fitting planet mass. However, relative core size is mostly determined by $\mathrm{Fe/Si_{bulk}}$.

Figure 7 indicates that the correlation between gas metallicity and atmospheric radius fraction is generally weakly negative. The upper bound on m_{env} positively correlates with Z_{env} (not shown). This is because the same atmospheric thickness of a more metal-rich gas can only be obtained by increasing atmospheric mass. Among the six exoplanets, the upper bound on m_{env} differs depending on bulk density and data uncertainty. Thus the five potentially rocky exoplanets (Figure 7 a-e) can have an atmosphere of maximum mass of 10^{-5}– 10^{-7} $\mathrm{M_\oplus}$ for low metallicities ($Z_{\mathrm{env}} < 0.2$). For high metallicities ($Z_{\mathrm{env}} > 0.8$), the maximum mass can be four magnitudes higher. In comparison the Earth's atmosphere has similar mass fraction of about 9×10^{-7} $\mathrm{M_\oplus}$. For the volatile-rich exoplanets (Figure 7 e-f), the correlation between the atmospheric radius fraction r_{env}/R and Z_{env} is strongest and the correlation between the upper bound on m_{env} and Z_{env} seems to be negative. Whether the planets could retain the constrained atmospheres with regard to possible photo-evaporative mass loss is not addressed in our model, but needs some post-analysis consideration (section 4.1).

Overall, correlations are generally weak since the problem addressed here is highly degenerate. In other words, an arbitrary change in 2 model parameters can be compensated by the remaining 6 model parameters in order to fit data. We find significant correlations between those model parameters that most strongly influence mass and/or radius and that countervail each other regarding this datum (e.g., r_{mantle} and m_{water} both most strongly affect planet mass).

Finally, the predicted ranges for structural parameters strongly depend on the specific planet data and associated uncertainties. Even though we see a distinction between the potentially rocky (HD 219134b, Kepler-10b, Kepler-93b, CoRoT-7b, 55 Cnc $\mathrm{e^S}$) and volatile-rich planet types (55 Cnc $\mathrm{e^L}$ and HD 97658b), the distributions can vary significantly among planets of the same type. Among all studied planets, Kepler-10b seems to be best constrained and its interior is most similar to an Earth-like structure. It is our contention that a case-by-case analysis is essential for a thorough characterization of planet interiors. A comparison of previous results (section 2) with our analysis shows very good agreement.

4.1. Evaporative mass loss

Highly irradiated planets can lose large amounts of their atmospheres through hydrodynamic mass loss driven by the extreme ultraviolet and X-ray heating from their host stars. In order to investigate whether our data-constrained interior structures are stable in the sense that atmospheres are stable against photo-evaporation, we use simplistic analytical relationships by Lopez & Fortney (2013) and Jin et al. (2014). A thorough analysis involving state-of-the-art mass loss models that couple hydrodynamic evaporation and thermal evolution models (e.g. Valencia et al. 2010) lies outside the scope of this study. Both simplistic scaling relations were fit against a large number of model runs and qualitatively describe the importance of mass loss but do not make detailed predictions. Lopez & Fortney (2013) provide a fit for threshold fluxes at which significant atmospheric loss occurs as a function of core mass and mass-loss efficiency for Earth-like, rocky interiors and H/He atmospheres (of up to 60 % in mass fraction). Similarly, Jin et al. (2014) provide a simplistic mass-radius-threshold below which planets have likely lost their entire H/He atmosphere. The application of both relationships to our posterior realizations suggest that all studied planets experience significant mass loss, except for HD 97658b (and mass-loss efficiencies below 0.05 regarding the Lopez & Fortney (2013) relationship). These findings are also in agreement with previous studies, e.g., namely with the suggestions of Valencia et al. (2010) that CoRoT-7b would likely not possess a significant atmosphere as well as Demory et al. (2016) that 55 Cnc e can be devoid of atmosphere.

In general, surface temperatures of the studied planets are high ($\sim$ 2000 K, depending on structure and planet case) which may imply molten rocks at the surface and outgassing from the planetary interior. Outgassing is a likely source for secondary atmospheres (e.g., Schaefer & Fegley 2007). However, due to the high irradiation, significant mass loss may remove most of such atmospheres. Detailed models are needed to determine how much vapor could remain in equilibrium with possible rates of outgassing and evaporative mass loss.

4.2. Sensitivity of structural parameters to bulk abundance constraints

Here, we examine the sensitivity of interior predictions on the spread of planetary bulk abundance constraints. We do this by testing how interior predictions for HD 219134b, 55 Cnc e, and HD 97658b vary in light of different bulk abundance estimates taken from: (I) best guess stellar abundance estimates, (II) iron-rich (V1), and (III) iron-poor (V2) abundance estimates (Table 3). Results are shown in Figure 8. The blue curves for the best guess abundance estimate refer to the same posterior pdfs previously shown in Figures 4–7.

The spread in interior parameters is largest for HD 219134b and smallest for HD 97658b. This is because the difference in bulk abundance constraints between V1 and V2 is a factor of 10 for HD 219134b, whereas for 55 Cnc e and HD 97658b the difference is only a factor of 4.5 and two, respectively. Except for

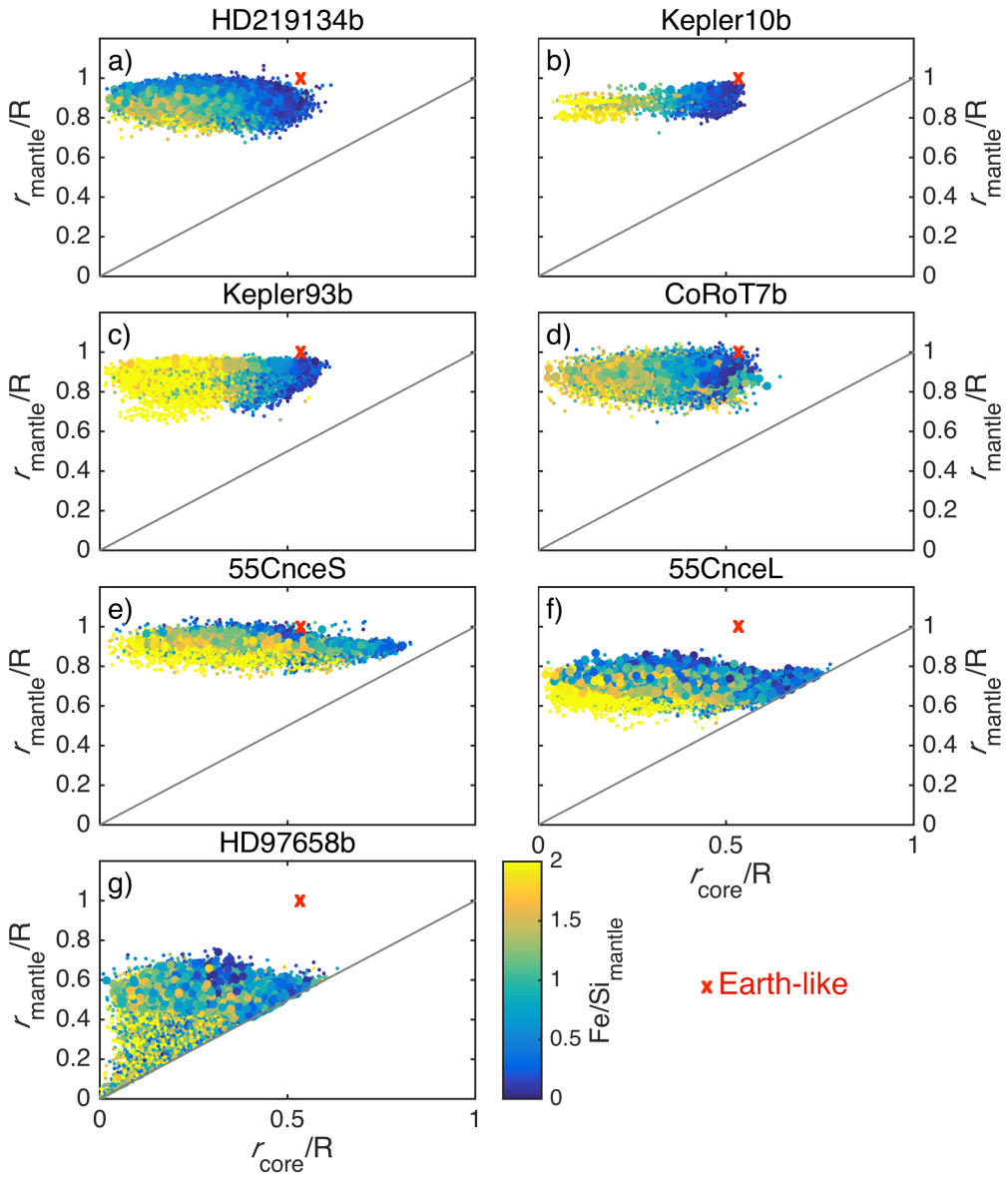

Fig. 4. Sampled two-dimensional (2-D) marginal posterior pdfs for the six selected exoplanets (a-f) showing the correlation between core and mantle sizes, $r_{\rm c}$, and $r_{\rm mantle}$ and mantle $\rm Fe/Si_{mantle}$. Bigger dots explain the data within 1-σ uncertainty. The straight line describes the lower limit of the mantle size where $r_{\rm mantle} = r_{\rm c}$. Earth-like parameters are depicted by the red cross.

$\rm Fe/Si_{mantle}$ and $r_{\rm c}$, differences between the cumulative distribution functions (cdfs) are generally minor. Compared to V2, the 50th-percentile in $r_{\rm c}$ and $\rm Fe/Si_{mantle}$ increases by up to 20 % and 200 % for V1, respectively, for $r_{\rm mantle}$ and $m_{\rm water}$ these variations are on the order of a few percents. Differences in $m_{\rm env}$ are minor.

The differences in core size and mantle composition introduced by the use of different stellar abundance estimates are even more pronounced when reduced uncertainties for mass and radius are available. This will be addressed in future parameter studies.

4.3. Direct versus non-direct stellar abundance proxy

Here, we investigate the influence of different stellar abundance proxies by comparing retrieved interior structures obtained with the direct ($\rm Fe/Si_{bulk} = Fe/Si_{star}$ and $\rm Mg/Si_{bulk} = Mg/Si_{star}$) and non-direct abundance proxy ($\rm Fe/Si_{bulk} = 10^{-5}\ Fe/Si_{star}$ and $\rm Mg/Si_{bulk} = 0.5\ Mg/Si_{star}$) (see section 3.2) on best guess stellar abundance estimates. The non-direct abundance proxy implies an extremely low bulk iron (nearly iron-free) content of the planets. With the constraint of a nearly iron-free planet, mass and radius of Kepler-93b and Kepler-10b can not be fit within 1-σ uncertainty. All other studied planets can be explained within 1-σ uncertainty, because data uncertainty is simply large enough or the bulk density (e.g., 55 Cnc $e^{\rm L}$ and HD 97658b) can be explained without a large iron core.

Figure 9 illustrates the differences in parameter estimates for the direct (blue curves) and non-direct (green curves) abundance proxy. Again, the blue curve refer to the same posterior pdfs previously shown in Figures 4–7, and Figure 8 (blue curve).

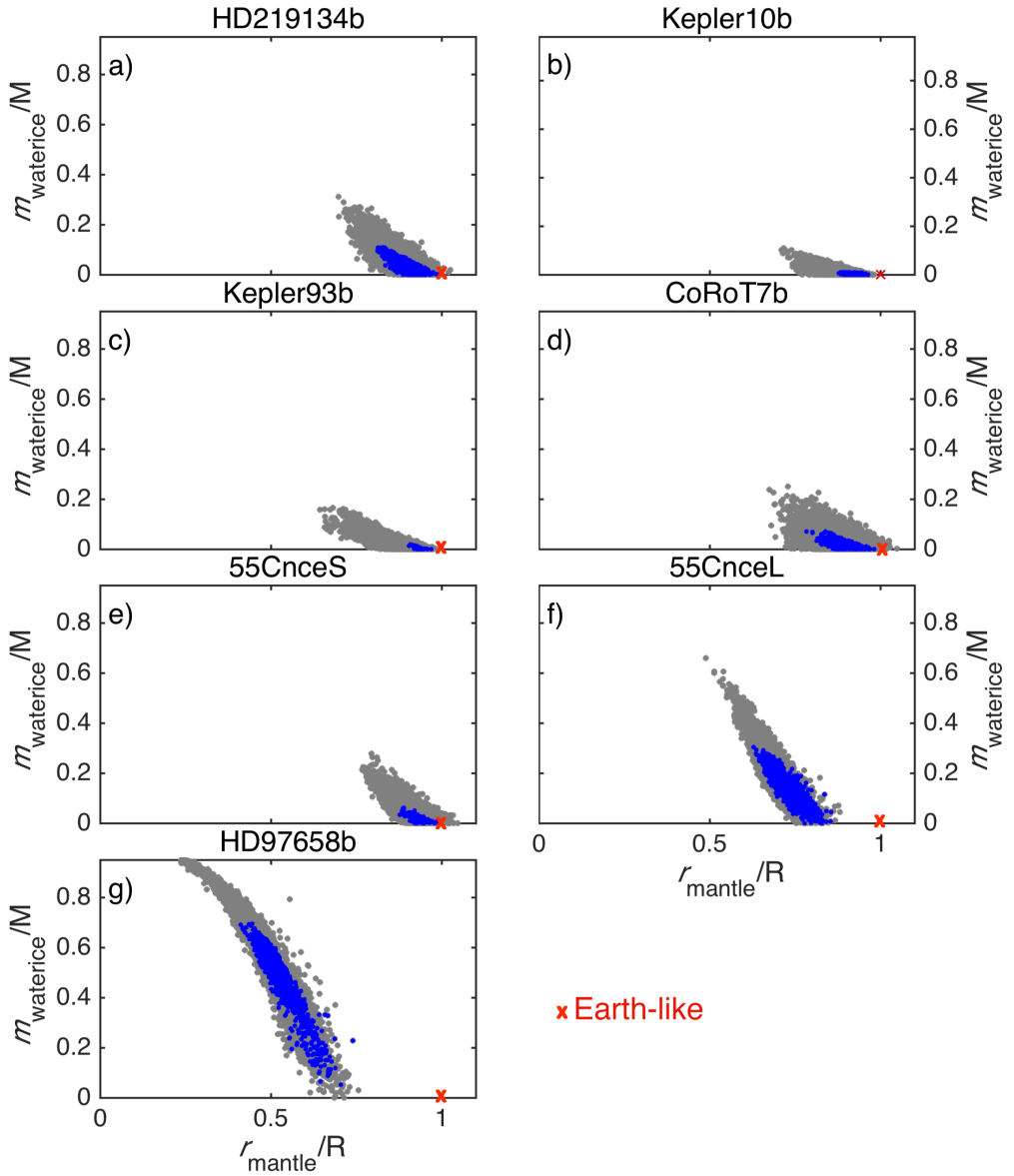

Fig. 5. Sampled 2-D marginal posterior pdfs for the six selected exoplanets (a-f) showing the correlation between mantle size $r_{\rm mantle}$ and mass of water $m_{\rm water}$. Blue points explain the data within 1-σ uncertainty. Earth-like parameters are depicted by the red cross.

The obtained structural parameters differ significantly between the two tested abundance proxies. As expected, using the non-direct abundance proxy compared to the direct abundance proxy leads to extremely low iron content in the mantle and tiny iron cores. In order to still fit mass, the size of rocky interior is larger. The 50th-percentiles of the parameter cdfs in Figure 9 change as follows for the extreme sub-stellar bulk abundance constraints:

- $r_{\rm c}$ decreases by 78% - 83%,
- $r_{\rm mantle}$ increases by 2% - 13%,
- $\rm Fe/Si_{mantle}$ decreases by 100%,
- $m_{\rm water}$ decreases by 9% - 50%,

Since structural variability in core and mantle is strongly restricted by the extremely low bulk abundance constraint, core and mantle parameters are generally better constrained (i.e., cdf curves are steeper).

With our methodology and the given data, such extreme sub-stellar abundances cannot be excluded for potentially rocky exoplanets, although extremely low iron content is disfavored for Kepler-93b and Kepler-10b. It is important to note that such low iron contents are very unlikely for volatile-rich planets, because accreted volatiles originate from primordial-disk regions beyond the ice-line at which also Mg-Fe-Si-bearing species condensed and likely reached the stellar ratio (Thiabaud et al. 2015).

In order to quantify how much the direct abundance proxy is preferred over the non-direct abundance proxy, we use the posterior odds, K, that is a multiplication of Bayes factor and prior odds (Jeffreys 1998):

$$K = \frac{\mathrm{p}(\mathbf{d}|H_{\rm d})\mathrm{p}(H_{\rm d})}{\mathrm{p}(\mathbf{d}|H_{\rm n})\mathrm{p}(H_{\rm n})} \ . \tag{2}$$

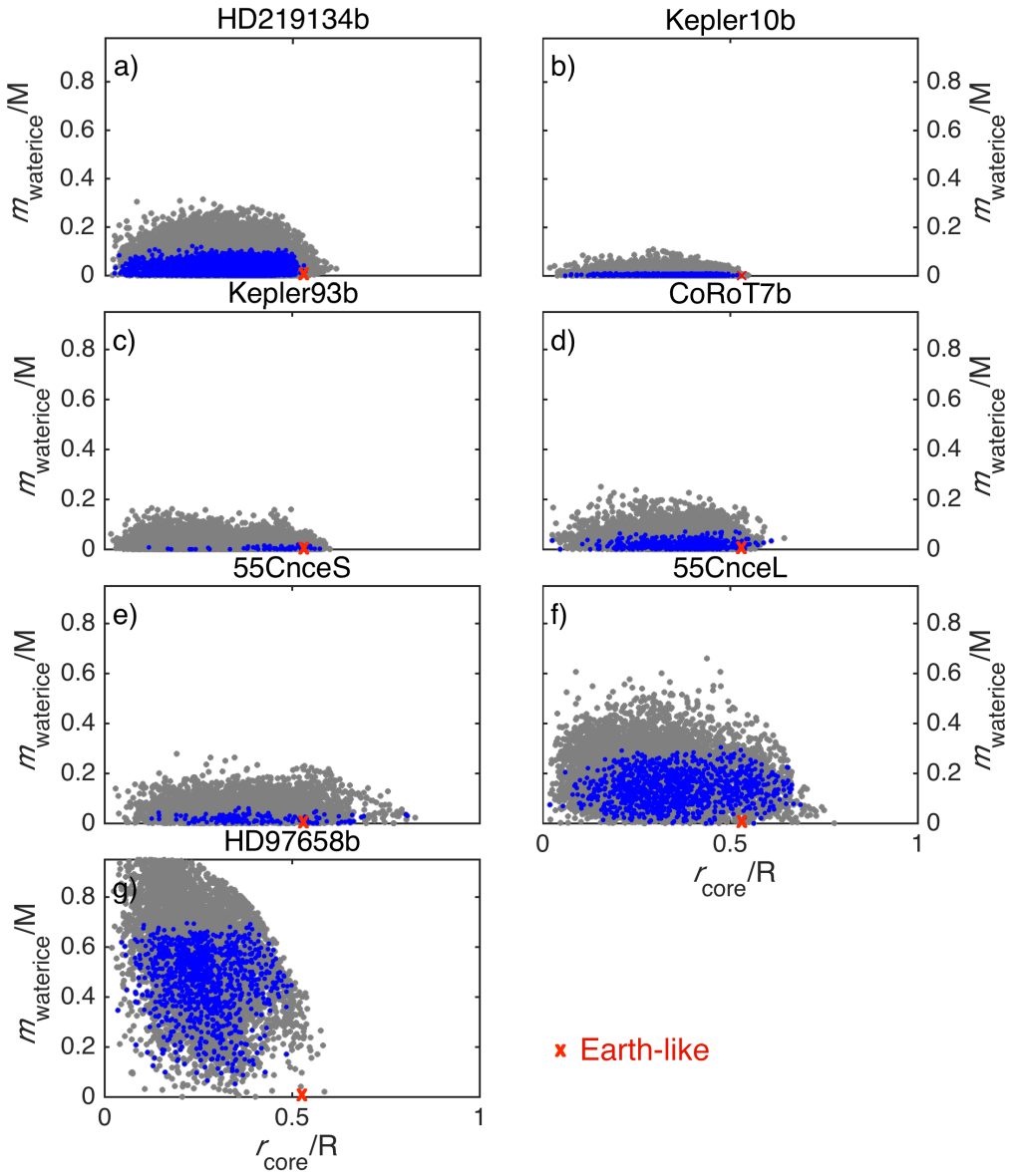

Fig. 6. Sampled 2-D marginal posterior pdfs for the six selected exoplanets (a-f) showing the correlation between core size r_c and mass of water m_{water}. Blue points explain the data within 1-σ uncertainty. Earth-like parameters are depicted by the red cross.

Here, H_d and H_n denote the hypothesis of validity of the direct and non-direct abundance proxy, respectively, and the probability

$$p(\mathbf{d}|H_d) = \int p(\mathbf{m}|H_d)p(\mathbf{d}|\mathbf{m}, H_d)d\mathbf{m}\,, \quad (3)$$

represents how well some data are explained under the assumption of a hypothesis H_d. Instead of the Bayes factor integral we use the maximum likelihood estimate. We obtain K-values around 10^1, except for Kepler-93b and Kepler-10b with K-values of 10^2. This means that only for Kepler-93b and Kepler-10b, there is a strong evidence that the direct abundance proxy better explains the planetary mass and radius.

Generally, it will be very difficult to study the validity of a direct correlation of relative bulk abundances between star and hosted exoplanet given usual data uncertainties. Further studies on solar system objects are needed to improve our understanding of such abundance correlations and their dependence on planet formation history.

5. Discussion of the assumptions

The success of an inference method is subject to the limitations and assumptions of the forward function $g(\cdot)$. Firstly, we consider pure iron cores, which may lead to a systematic overestimation of core density and thus an underestimation of core size, if volatile compounds in the core are significant. The trade-off between predicted and independently inferred core sizes can be on the order of few to tens of percents, as shown for the terrestrial solar system planets in Dorn et al. (2015).

Secondly, our approach assumes sub-solidus conditions for core and mantle as well as a perfectly known EoS parameters for all considered compositions. For the six exoplanets consid-

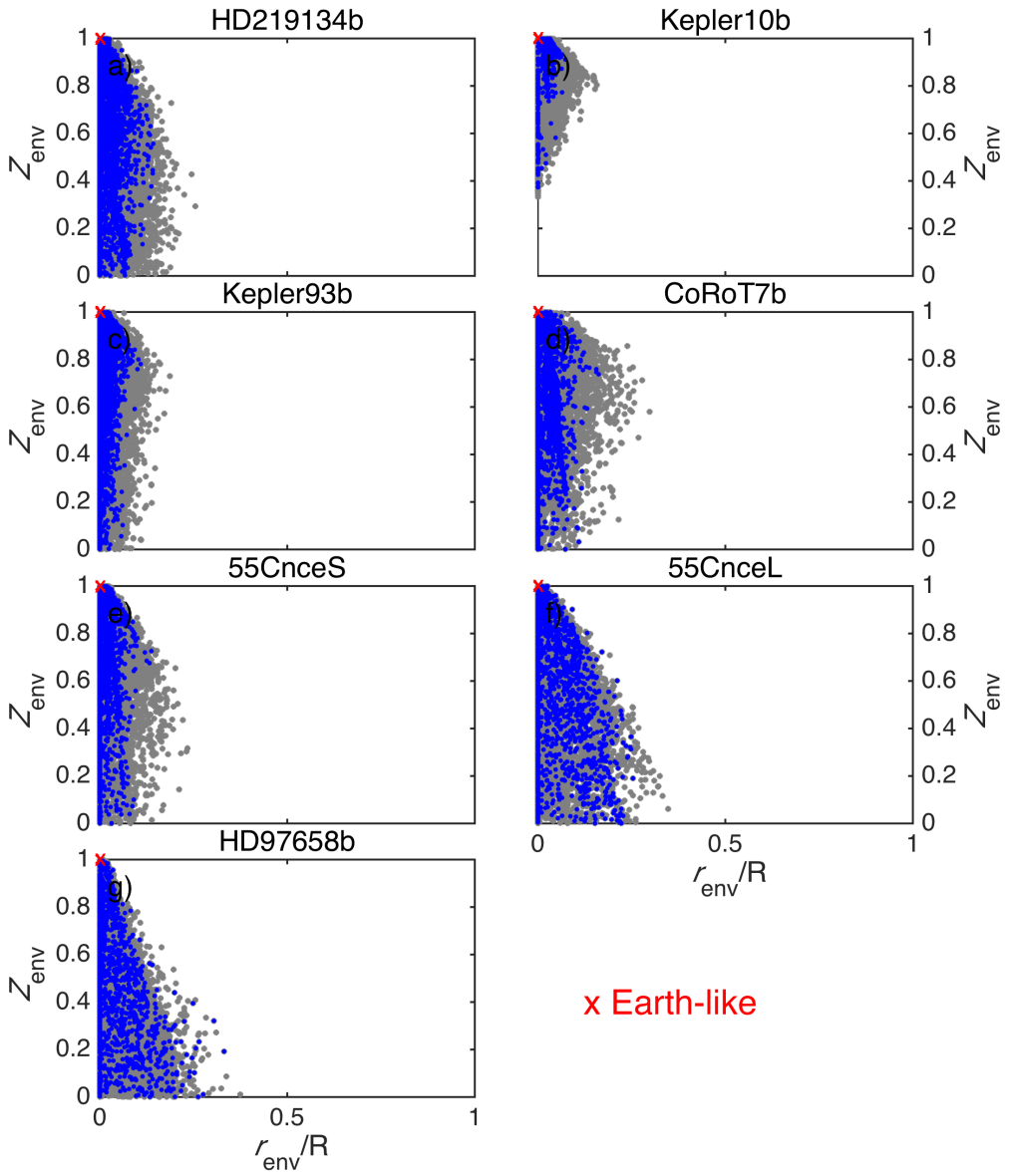

Fig. 7. Sampled 2-D marginal posterior pdfs for the six selected exoplanets (a-f) showing the correlation between gas metallicity $Z_{\rm env}$ and atmospheric radius fraction r_{env}/R. Blue points explain the data within 1-σ uncertainty. Earth-like parameters are depicted by the red cross.

ered here, their pressures and temperatures exceed the ranges for which these parameters can be measured in the laboratory. Clearly, extrapolations introduce uncertainty.

Thirdly, we have assumed pure water composition of the ice layer, but other compounds such as CO, CO_2, CH_4, NH_3, etc. are also possible since the additional elements are relatively abundant. We have used water as a proxy for these volatiles in general because (1) oxygen is more abundant than carbon and nitrogen in the universe, and (2) water condenses at higher temperatures than ammonia and methane.

Fourthly, our atmospheric model uses prescribed opacities of Jin et al. (2014), which is suitable for solar abundances. In this aspect, the prescription is therefore not self-consistent with the non-solar metallicity cases we present in this work. We have checked that using different infrared and/or visible opacities can introduce errors in radius of $\sim$5 %. Models that compute line-by-line opacities with their corresponding atmospheric abundances should be performed in the future to compute planetary radii in a self-consistent way. Another aspect is our assumption of ideal gas behavior. We have checked that for atmospheric mass fractions ($m_{\rm env}/M$) of up to 1 %, the difference in the radius between using the Saumon et al. (1995) EOS and ideal gas (for H-He atmospheres) can reach 10 %. For the vast majority of our results, atmospheric mass fractions are smaller than 0.1 %, and thus the ideal gas assumption does not introduce a remarkable flaw.

Since our interior models are static, evolutionary effects on the interior structure are not accounted for in the forward model. As demonstrated in section 4.1, constraints on evolutionary processes such as thermal mass loss of gaseous layers can be roughly approximated by post-analysis considerations. We have used very approximate analytic scaling laws from Lopez & Fortney (2013) and Jin et al. (2014) to rule out gas-rich planet realizations.

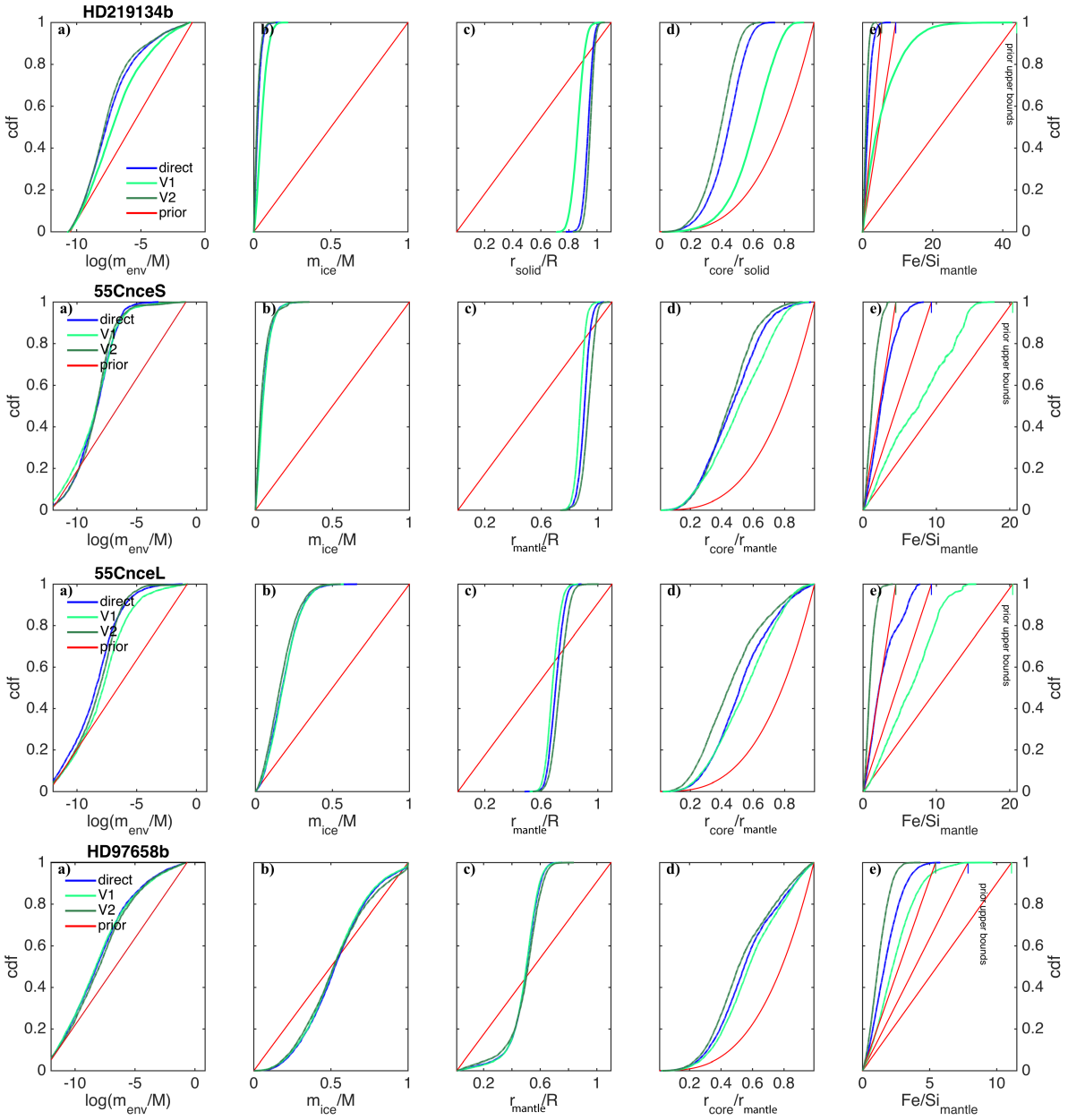

Fig. 8. Application of V0, V1, and V2 stellar abundance estimates: cdfs of sampled 1D marginal posterior (green to blue) and prior (red) for HD 219134b, 55 Cnc e^{S}, 55 Cnc e^{L}, and HD 97658b: (a) $m_{\rm water}$, (c) $r_{\rm mantle}$, (d) $r_{\rm c}$, and (e) $\rm Fe/Si_{mantle}$. Posterior cdfs refer to the different host star abundance estimates (V1- iron rich, V2 - iron poor) listed in Table 3. The dashed lines are the 95 % lower and upper confidence bounds, which almost completely overlap the solid lines. Depending on the stellar abundance proxy estimates, the upper prior bound in (e) differs, which is indicated by the vertical colored lines corresponding to the respective proxy.

6. Summary

We have presented the application of a generalized Bayesian inference method from Dorn et al. (2017) in order to constrain the general interior structure of six selected super Earths: HD 219134b, Kepler-10b, Kepler-93b, CoRoT-7b, 55 Cnc e, and HD 97658b. Their available data are mass, radius, and bulk abundance constraints on relative refractory elements (Fe, Mg, Si) measured in the photosphere of their host stars. We assume a general structure of core, mantle, ice and gas for which we constrain core size, mantle thickness and composition, mass of water, and key characteristics of the atmosphere (mass, intrinsic luminosity, composition). We have investigated the sensitivity of the constrained interior parameters on the spread of bulk abundance estimates as determined by research groups with different techniques (Hinkel et al. 2014). We have also determined how predictions of interior parameters are affected by a very non-direct correlation of relative abundances between star and planet, compared to a direct correlation. Our findings are summarized as follows:

- The available data of the six studied exoplanets enables us to constrain interior structure and to determine parameter correlations. Depending on data and data uncertainty, the ability of constraining interior structure differs. Kepler-10b appears to be best constrained, since data uncertainties are relatively small.
- In general, correlations between interior parameters are weak. We find strongest 2-D correlations between the size of the rocky interior $r_{\rm mantle}$ and water mass fraction $m_{\rm water}$.

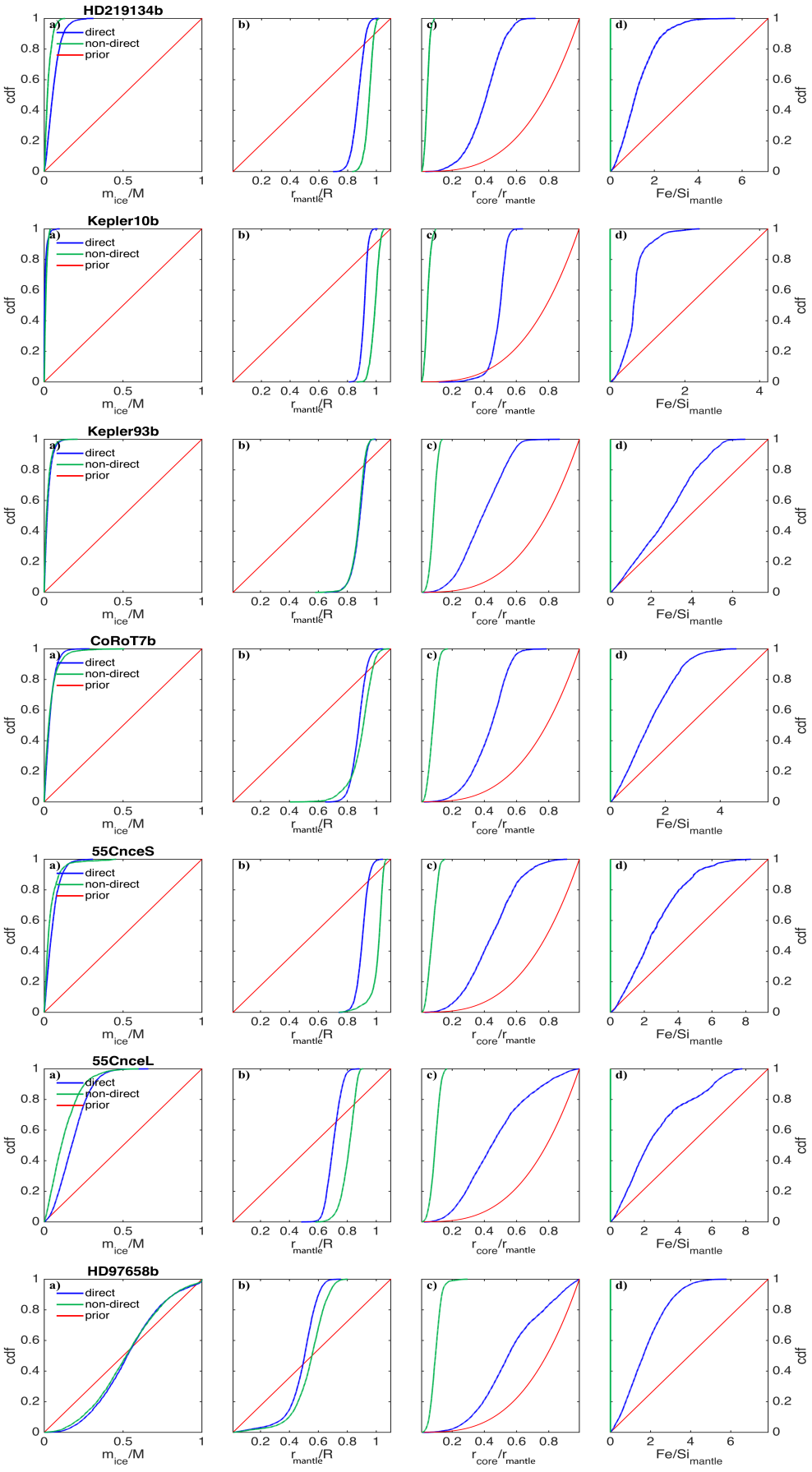

Fig. 9. Application of direct and non-direct abundance proxies: cdfs of 1D marginal posterior pdfs and prior pdfs for HD 219134b, Kepler-10b, Kepler-93b, CoRoT-7b, 55 Cnc e^{S}, 55 Cnc e^{L}, and HD 97658b: (a) $m_{\rm env}$, (b) $Z_{\rm env}$, (c) $m_{\rm water}$, (d) $r_{\rm mantle}$, (e) $r_{\rm c}$. Prior (red), posterior pdf in blue and green for direct and non-direct stellar-planetary abundance correlation, respectively. See discussion in section 4.3.

- We determine an upper range of possible atmospheric masses that positively correlate with gas metallicity. Whether the planets can retain the constrained atmospheres with regard to the high irradiation of their host stars is evaluated with simplistic analytical relationships that determine the importance of photo-evaporative mass loss.
- The data of most of the studied exoplanets can not exclude massive amounts of water. Even for the potentially rocky exoplanets, the possible range of water mass fraction can reach up to 35 %, depending on the planet. Only for Kepler-10b, a massive water mass fraction can be excluded ($m_{\rm water}/M < 1$ %).
- Discrepancies in the stellar abundance estimates that are used as proxies for planetary bulk abundance mainly affect the prediction of mantle composition and core size. Effects on the other parameters of atmosphere, water layer, and size of rocky interior are small.
- Extremely sub-stellar abundance constraints are less in agreement with mass and radius data for the potentially rocky exoplanets, but cannot be excluded without additional considerations. For instance, potentially volatile-rich exoplanets likely accreted material that originated from regions beyond the ice line, where Fe-Mg-Si bearing species reached stellar ratios.

Available mass and radius data of exoplanets cannot be used to verify whether a correlation between stellar and planetary relative abundances of Fe, Mg, and Si differs from a direct 1:1 correlation. This is because degeneracy in interior structure of exoplanets is too large. More detailed studies of terrestrial solar system planets, e.g. Mars and Venus, would greatly help to improve our understanding of the discussed abundance constraints.

In order to rigorously characterize interior structure for an exoplanet, it is crucial to perform a case-by-case inference method, since constrained interior distributions highly depend on data and data uncertainties. The range of possible exoplanet interiors is large, since the problem is highly degenerate. Commonly used mass-radius-curves of idealized compositions for comparison against observed masses and radii can only serve as a rough planet characterization. Bayesian inference methods offer a powerful way to determine exoplanet interiors sensibly.

Acknowledgements. This work was supported in part by the Swiss National Foundation under grant 15-144. It was in part carried out within the frame of the National Centre for Competence in Research PlanetS. We would like to thank James Connolly for informed discussions, Amaury Thiabaud for making available the data published in Thiabaud et al. (2015). N.R.H would like to thank CHW3. The results reported herein benefited from collaborations and/or information exchange within NASA's Nexus for Exoplanet System Science (NExSS) research coordination network sponsored by NASA's Science Mission Directorate.

Appendix A: Element abundance notations

Typically in astronomy, the total number of absorbing atoms is scaled with respect to hydrogen (or 10^{12} atoms), which is the most common element in the universe. Geologists often use 10^6 silicon atoms as a scalar. In addition, the abundance ratio within the star is referenced to the same element abundance ratio within the Sun, the most well measured star, such that the star can be defined to be rich, poor, or solar-like with respect to that element. The unit of dex is described in mathematical terms as:

$$[X/H] = \log(N_X/N_H)_{star} - \log(N_X/N_H)_{Sun}\,, \qquad \text{(A.1)}$$

where N_X and N_H are the number of element X and hydrogen atoms per unit volume, respectively. When an abundance ratio is given in square brackets, it denotes that it is in reference to the Sun. The majority of our discussion is with respect to abundance mass ratios without reference to the Sun, X/H (see Table 3, columns 3 and 4).

References

Allende Prieto, C., Barklem, P. S., Lambert, D. L., & Cunha, K. 2004, S4N: A spectroscopic survey of stars in the solar neighborhood. The Nearest 15 pc. Astronomy & Astrophysics, 420, 183.

Batalha, N. M., Borucki, W. J., Bryson, S. T., Buchhave, L. A., Caldwell, D. A., Christensen-Dalsgaard, J., ... & Gilliland, R. L. 2011, Kepler's first rocky planet: Kepler-10b. The Astrophysical Journal, 729(1), 27.

Bond, J. C., Tinney, C. G., Butler, R. P., Jones, H. R. A., Marcy, G. W., Penny, A. J., & Carter, B. D. 2006, The abundance distribution of stars with planets. Monthly Notices of the Royal Astronomical Society, 370, 163.

Bond, J. C., O'Brien, D. P., & Lauretta, D. S. 2010, The compositional diversity of extrasolar terrestrial planets. I. In situ simulations. The Astrophysical Journal, 715(2), 1050.

Bouchet, J., Mazevet, S., Morard, G., Guyot, F., & Musella, R. 2013, Ab initio equation of state of iron up to 1500 Gpa. Physical Review B, 87(9), 094102.

Burrows, A. S. 2014. Highlights in the study of exoplanet atmospheres. Nature, 513(7518), 345-352.

Connolly, J. A. D. 2009, The geodynamic equation of state: what and how. Geochemistry, Geophysics, Geosystems, 10(10).

Delgado Mena, E., Israelian, G., González Hernández, J. I., Bond, J. C., Santos, N. C., Udry, S., & Mayor, M. 2010, Chemical Clues on the Formation of Planetary Systems: C/O Versus Mg/Si for HARPS GTO Sample. The Astrophysical Journal, 725, 2349.

Demory, B. O., Gillon, M., de Wit, J., Madhusudhan, N., Bolmont, E., Heng, K., ... & Stamenković, V. 2016, A map of the large day–night temperature gradient of a super-Earth exoplanet. Nature.

Demory, B. O., Gillon, M., Madhusudhan, N., & Queloz, D. 2015, Variability in the super Earth 55 Cnc e. arXiv preprint arXiv:1505.00269.

Dorn, C., Khan, A., Heng, K., Connolly, J.A.D., Alibert, Y., Benz, W., and Tackley, P., 2015. Can we constrain the interior structure of rocky exoplanets from mass and radius measurements?, Astronomy&Astrophysics, 577, A83.

Dorn, C., Venturini, J., Khan, A., Heng, K., Alibert, Y., Helled, R., Rivoldini, A., Benz, W. (2017). A Generalized Bayesian Inference Method for Constraining the Interiors of Super Earths and Sub-Neptunes, 2017, Astronomy&Astrophysics, 597, A37.

Dragomir, D., Matthews, J. M., Eastman, J. D., Cameron, C., Howard, A. W., Guenther, D. B., ... & Weiss, W. W. 2013, MOST detects transits of HD 97658b, a warm, likely volatile-rich super Earth. The Astrophysical Journal Letters, 772(1), L2.

Drake, M. J., & Righter, K. 2002, Determining the composition of the Earth. Nature, 416(6876), 39-44.

Dressing, C. D., Charbonneau, D., Dumusque, X., Gettel, S., Pepe, F., Cameron, A. C., ... & Watson, C. 2015, The mass of Kepler-93b and the composition of terrestrial planets. The Astrophysical Journal, 800(2), 135.

Elser, S., Meyer, M. R., & Moore, B. 2012, On the origin of elemental abundances in the terrestrial planets. Icarus, 221(2), 859-874.

Endl, M., Robertson, P., Cochran, W. D., MacQueen, P. J., Brugamyer, E. J., Caldwell, C., ... & Gullikson, K. 2012, Revisiting ρ1 Cancri e: A new mass determination of the transiting super Earth. The Astrophysical Journal, 759(1), 19

Fortney, J. J., Marley, M. S., & Barnes, J. W. 2007, Planetary radii across five orders of magnitude in mass and stellar insolation: application to transits. The Astrophysical Journal, 659(2), 1661.

Gillon, M., Demory, B. O., Benneke, B., Valencia, D., Deming, D., Seager, S., ... & Udry, S. 2012, Improved precision on the radius of the nearby super Earth 55 Cnc e. Astronomy & Astrophysics, 539, A28

Gonzalez, G., Laws, C., Tyagi, S., & Reddy, B. E. 2001, Parent Stars of Extrasolar Planets. VI. Abundance Analyses of 20 New Systems. The Astronomical Journal, 121, 432

Gonzalez, G. 1997, The stellar metallicity—giant planet connection. MNRAS, 285, 403

Gordon, S., & McBride, B. 1994, Computer program for calculation of complex chemical equilibrium compositions and applications. Cleveland, Ohio, Springfield, Va: National Aeronautics and Space Administration, Office of Management, Scientific and Technical Information Program; National Technical Information Service, distributor

Grasset, O., Schneider, J., & Sotin, C. 2009, A study of the accuracy of mass-radius relationships for silicate-rich and ice-rich planets up to 100 Earth masses. The Astrophysical Journal, 693(1), 722.

Guillot, T. 2010, On the radiative equilibrium of irradiated planetary atmospheres. Astronomy & Astrophysics, 520, A27.
Hinkel, N. R., Timmes, F. X., Young, P. A., Pagano, M. D., & Turnbull, M. C. 2014, Stellar Abundances in the Solar Neighborhood: The Hypatia Catalog. The Astronomical Journal, 148, 54.
Howe, A. R., Burrows, A. S., & Verne, W. 2014, Mass-radius relations and core-envelope decompositions of super Earths and sub-Neptunes. The Astrophysical Journal, 787(2), 173.
Jeffreys, H. (1998). The theory of probability. OUP Oxford.
Jin, S., Mordasini, C., Parmentier, V., van Boekel, R., Henning, T., & Ji, J. 2014, Planetary population synthesis coupled with atmospheric escape: a statistical view of evaporation. The Astrophysical Journal, 795(1), 65.
Johnson, T. V., Mousis, O., Lunine, J. I., & Madhusudhan, N. 2012, Planetesimal compositions in exoplanet systems. The Astrophysical Journal, 757(2), 192.
Kang, W., Lee, S.-G., & Kim, K.-M. 2011, Abundances of Refractory Elements for G-type Stars with Extrasolar Planets. The Astrophysical Journal, 736, 87
Khan, A., & Connolly, J. A. D. 2008, Constraining the composition and thermal state of Mars from inversion of geophysical data. Journal of Geophysical Research: Planets (1991–2012), 113(E7).
Kurokawa, H., & Kaltenegger, L. 2013, Atmospheric mass-loss and evolution of short-period exoplanets: the examples of CoRoT-7b and Kepler-10b. Monthly Notices of the Royal Astronomical Society, stt965.
Kuskov, O. L., & Kronrod, V. A. 2001, Core sizes and internal structure of Earth's and Jupiter's satellites. Icarus, 151(2), 204–227.
Lodders, K. 2003, Solar system abundances and condensation temperatures of the elements. The Astrophysical Journal, 591(2), 1220.
Lodders, K., & Fegley, B. 2002, Atmospheric chemistry in giant planets, brown dwarfs, and low-mass dwarf stars: I. Carbon, nitrogen, and oxygen. Icarus, 155(2), 393-424.
Lodders, K., Plame, H., & Gail, H.-P. 2009, Landolt-Börnstein - Group VI Astronomy and Astrophysics Numerical Data and Functional Relationships in Science and Technology Volume 4B: Solar System. Edited by J.E. Trümper, 4B, 44.
Lopez, E. D., & Fortney, J. J. 2013, The role of core mass in controlling evaporation: the Kepler radius distribution and the Kepler-36 density dichotomy. The Astrophysical Journal, 776(1), 2.
Luck, R. E., & Heiter, U. 2005, Stars within 15 Parsecs: Abundances for a Northern Sample. The Astronomical Journal, 129, 1063.
Lyon, S. P., & Johnson, J. D. 1992, LANL Rep. LA-UR-92-3407 (Los Alamos: LANL).
Marcus, R. A., Stewart, S. T., Sasselov, D., & Hernquist, L. 2009, Collisional stripping and disruption of super Earths. The Astrophysical Journal Letters, 700(2), L118.
Madhusudhan, N. 2012, C/O ratio as a dimension for characterizing exoplanetary atmospheres. The Astrophysical Journal, 758(1), 36.
McDonough, W. F., & Sun, S. S. 1995, The composition of the Earth. Chemical geology, 120(3), 223–253.
Mishenina, T., Gorbaneva, T., Pignatari, M., Thielemann, F.-K., & Korotin, S. A. 2015, Mn abundances in the stars of the Galactic disc with metallicities -1.0 < [Fe/H] < 0.3. Monthly Notices of the Royal Astronomical Society, 454, 1585
Mishenina, T. V., Soubiran, C., Kovtyukh, V. V., & Korotin, S. A. 2004, On the correlation of elemental abundances with kinematics among galactic disk stars. Astronomy & Astrophysics, 418, 551.
Mishenina, T. V., Soubiran, C., Bienaymé, O., Korotin, S. A., Belik, S. I., Usenko, I. A., & Kovtyukh, V. V. 2008, Spectroscopic investigation of stars on the lower main sequence. Astronomy & Astrophysics, 489, 923.
Mishenina, T. V., Pignatari, M., Korotin, S. A., Soubiran, C., Charbonnel, C., Thielemann, F.-K., ...& Basak, N. Y. 2013, Abundances of neutron-capture elements in stars of the Galactic disk substructures. Astronomy & Astrophysics, 552, A128
Morgan, J. W., & Anders, E. 1980, Chemical composition of earth, Venus, and Mercury. Proceedings of the National Academy of Sciences, 77(12), 6973–6977.
Mortier, A., Santos, N. C., Sousa, S. G., Fernandes, J. M., Adibekyan, V. Z., Delgado Mena, E., Montalto, M., & Israelian, G. 2013, Astronomy & Astrophysics, 558, A106.
Mosegaard, K., & Tarantola, A. 1995, Monte Carlo sampling of solutions to inverse problems. Journal of Geophysical Research, 100(B7), 12431–12447.
Motalebi, F., Udry, S., Gillon, M., Lovis, C., Ségransan, D., Buchhave, L. A., ...& Rice, K. 2015. The HARPS-N Rocky Planet Search-I. HD 219134 b: A transiting rocky planet in a multi-planet system at 6.5 pc from the Sun. Astronomy & Astrophysics, 584, A72.
Neves, V., Santos, N. C., Sousa, S. G., Correia, A. C. M., & Israelian, G. 2009, Chemical abundances of 451 stars from the HARPS GTO planet search program. Thin disc, thick disc, and planets. Astronomy & Astrophysics, 497, 563.
Newsom, H. E. 1995, Composition of the solar system, planets, meteorites, and major terrestrial reservoirs. In Global earth physics: a handbook of physical constants (Vol. 1, p. 159). Amer. Geophys. Union.
Ramírez, I., Prieto, C. A., & Lambert, D. L. 2007, Oxygen abundances in nearby stars. Astronomy & Astrophysics, 465, 271
Rogers, L. A. 2015, Most 1.6 Earth-radius planets are not rocky. The Astrophysical Journal, 801(1), 41.
Rogers, L. A., & Seager, S. 2010, A framework for quantifying the degeneracies of exoplanet interior compositions. The Astrophysical Journal, 712(2), 974.
Rogers, L. A., Bodenheimer, P., Lissauer, J. J., & Seager, S. 2011, Formation and structure of low-density exo-Neptunes. The Astrophysical Journal, 738(1), 59.
Santos, N. C., Adibekyan, V., Mordasini, C., Benz, W., Delgado-Mena, E., Dorn, C., ... & Udry, S. 2015, Constraining planet structure from stellar chemistry: the cases of CoRoT-7, Kepler-10, and Kepler-93. Astronomy & Astrophysics, 580, L13.
Saumon, D., Chabrier, G., & Van Horn, H. M. (1995). An equation of state for low-mass stars and giant planets. The Astrophysical Journal Supplement Series, 99, 713.
Schaefer, L., & Fegley, B. 2007, Outgassing of ordinary chondritic material and some of its implications for the chemistry of asteroids, planets, and satellites. Icarus, 186(2), 462-483.
Seager, S., Kuchner, M., Hier-Majumder, C. A., & Militzer, B. 2007, Mass-radius relationships for solid exoplanets. The Astrophysical Journal, 669(2), 1279.
Shi, J. R., Gehren, T., & Zhao, G. 2004, Sodium abundances in nearby disk stars. Astronomy & Astrophysics, 423, 683.
Takeda, Y. 2007, Fundamental Parameters and Elemental Abundances of 160 F–G–K Stars Based on OAO Spectrum Database. Publications of the Astronomical Society of Japan, 59, 335.
Thevenin, F. 1998, Chemical Abundances in Late-Type Stars (VizieR On-line Data Catalog).
Thévenin, F., & Idiart, T. P. 1999, Stellar Iron Abundances: Non-LTE effects. The Astrophysical Journal, 521, 753.
Thiabaud, A., Marboeuf, U., Alibert, Y., Leya, I., & Mezger, K. 2015, Elemental ratios in stars vs planets. Astronomy & Astrophysics, 580, A30.
Thompson, S. L., & Lauson, H. S. 1972, Improvements in the Chart D radiation-hydrodynamic CODE III: revised analytic equation of state: Albuquerque, N. Mex., USA, Sandia Laboratories. Report SC-RR-71-0714.
Tsiaras, A., Rocchetto, M., Waldmann, I. P., Venot, O., Varley, R., Morello, G., ... & Tennyson, J. (2016). Detection of an atmosphere around the super Earth 55 Cancri e. arXiv preprint arXiv:1511.08901.
Valencia, D., Ikoma, M., Guillot, T., & Nettelmann, N. 2010, Composition and fate of short-period super Earths-The case of CoRoT-7b. Astronomy & Astrophysics, 516, A20.
Valencia, D., Sasselov, D. D., & O'Connell, R. J. 2007, Detailed Models of super Earths: How Well Can We Infer Bulk Properties? The Astrophysical Journal, 665(2), 1413.
Valenti, J. A., & Fischer, D. A. 2005, Spectroscopic properties of cool stars (SPOCS). I. 1040 F, G, and K dwarfs from Keck, Lick, and AAT planet search programs. The Astrophysical Journal Supplement Series, 159, 141.
Van Grootel, V., Gillon, M., Valencia, D., Madhusudhan, N., Dragomir, D., Howe, A. R., ... & Lovis, C. 2014, Transit confirmation and improved stellar and planet parameters for the super Earth HD 97658 b and its host star. The Astrophysical Journal, 786(1), 2.
Vazan, A., Kovetz, A., Podolak, M., & Helled, R. 2013, The effect of composition on the evolution of giant and intermediate-mass planets. Monthly Notices of the Royal Astronomical Society, stt1248.
Venturini, J., Alibert, Y., Benz, W., & Ikoma, M. 2015, Critical core mass for enriched envelopes: the role of H2O condensation. Astronomy & Astrophysics, 576, A114.
Wagner, F. W., Tosi, N., Sohl, F., Rauer, H., & Spohn, T. 2012, Rocky super Earth interiors-Structure and internal dynamics of CoRoT-7b and Kepler-10b. Astronomy & Astrophysics, 541, A103.
Weiss, L. M., Rogers, L. A., Isaacson, H. T., Agol, E., Marcy, G. W., Rowe, J. F., ... & Clark Fabrycky, D. 2015, Revised Masses and Densities of the Planets around Kepler-10. In AAS/Division for Extreme Solar Systems Abstracts (Vol. 3, p. 10102).
Winn, J. N., Matthews, J. M., Dawson, R. I., Fabrycky, D., Holman, M. J., Kallinger, T., ... & Moffat, A. F. 2011, A super Earth transiting a naked-eye star. The Astrophysical Journal Letters, 737(1), L18.